Interactions between plastic deformation and precipitation in Aluminium alloys: A crystal plasticity model

DOI:
10.1016/j.actamat.2023.118735

Document Version
Final published version

Acta Materialia 247 (2023) 118735

Contents lists available at ScienceDirect

Acta Materialia

journal homepage: www.elsevier.com/locate/actamat

Full length article

Interactions between plastic deformation and precipitation in Aluminium alloys: A crystal plasticity model

Madeleine Bignon, Ziyu Ma, Joseph D. Robson *, Pratheek Shanthraj[1]

Henry Royce Institute for Advanced Materials, The University of Manchester, Manchester, M193PL, UK

ARTICLE INFO

Keywords:
Dynamic precipitation
Growth and coarsening kinetics
Deformation localisation
Precipitation localisation
KWN model
Mechanical properties

ABSTRACT

This work presents a crystal plasticity model for dynamic precipitation in aluminium alloys. It takes into account both the influence of an evolving precipitate distribution on the critical stress for dislocation glide, and the accelerating effect of deformation on precipitation kinetics. The effect of precipitates on deformation behaviour is integrated into the crystal plasticity constitutive law. The effect of deformation on precipitation kinetics is modelled spatio-temporally using a multi-class precipitation kinetic model (KWN) incorporating the effect of deformation through accelerated solute diffusion caused by the production of excess vacancies. The model is applied to growth and coarsening of shearable precipitates in pre-aged AA7075 alloy under deformation at 150°C, which corresponds to an industrially relevant production. This paper first explores the influence of dynamic precipitation on the tensile behaviour, showing that dynamic precipitation might be responsible for a gain in uniform elongation and tensile stress of respectively 2% strain and 50 MPa for the case at hand. The influence of dynamic precipitation on the development of plastic strain heterogeneities is discussed. The model demonstrates how spatial heterogeneities in precipitate distribution may develop during deformation, and how these heterogeneities correlate with the development of strain heterogeneities. The precipitate distributions obtained under static or dynamic ageing are predicted and compared with each other, and the influence of texture is discussed.

1. Introduction

Age-hardened Al–Zn–Mg–Cu alloys from the 7xxx series are a promising material class for many engineering applications because of their light weight and high strength. The main reason for their strength is the presence of reinforcing precipitates, formed during a controlled heat treatment. The processing of age-hardened alloys usually involves an ageing treatment at intermediate temperature (80–150°C) during which the solute atoms diffuse and cluster to form precipitates. By acting as obstacles for dislocation motion, these precipitates reinforce the material.

While precipitates affect deformation, deformation also affects precipitation kinetics, by considerably accelerating solute transport [1–5]. Deformation influences precipitation through different mechanisms, including heterogeneous nucleation on dislocations [6], ballistic transport of solute atoms by dislocation glide, and production of excess vacancies, generated by the non-conservative motion of jogs on screw dislocations [7]. These deformation induced excess vacancies increase the mobility of solid solution atoms and therefore enhance diffusion. In the case of aluminium alloys and for temperatures lower than 200°C, excess vacancy production has been shown to play the most important role in diffusivity enhancement [8].

The interactions between precipitation and deformation, known as dynamic precipitation, are of practical importance. Recently, there has been a growing interest in taking advantage of this phenomenon to integrate the forming of the part and the ageing heat treatment. This consists in deforming the material at moderate temperature (100 to 200 °C) to give it its final shape, while precipitates form and grow, and confer the material its strength. The potential advantages of such an operation are multiple. First of all, due to the deformation induced enhanced solute diffusivity, the heat treatment duration can be significantly reduced if deformation and precipitation treatment are accomplished concurrently [9]. Further, formability can be greatly improved if the sample is given its shape at temperatures higher than room temperature. Additionally, it has recently been shown that under certain conditions, the precipitate distribution achieved under deformation could lead to improved mechanical properties compared to static ageing, with deformation resulting in a higher uniform elongation, without inducing any loss in the ultimate tensile strength [9]. In order

* Corresponding author.
E-mail address: joseph.d.robson@manchester.ac.uk (J.D. Robson).
[1] Now at United Kingdom Atomic Energy Authority, Culham, Abingdon, United Kingdom.

https://doi.org/10.1016/j.actamat.2023.118735
Received 8 September 2022; Received in revised form 20 January 2023; Accepted 29 January 2023
Available online 2 February 2023

to fully exploit the potential of dynamic precipitation, it is important to understand the coupled effects of deformation and precipitation. Typically, the warm forming operation will be performed on material that has been subject to a stabilisation pre-temper and/or a slow pre-heat to the forming temperature. In such cases, precipitate nucleation mainly occurs without dynamic effects during these initial steps, and the problem is reduced to understanding the influence of deformation on a pre-existing precipitate population.

The effect of precipitates on deformation can be described by different models, reviewed for example in [10]. While the smallest precipitates are sheared by dislocations, larger precipitates cause dislocations to bend around them and eventually form loops, during a process known as Orowan by-passing [11]. The influence of such precipitate-dislocation interactions on the yield stress is well captured by simple analytical models [11,12], that can account for the effect of a full particle size distribution [13].

While simple analytical models allow to calculate the contribution of precipitate hardening to the yield stress, embedding precipitation models in crystal plasticity (CP) simulations takes a step further in describing how precipitates affect deformation with greater fidelity. CP models rely on the constitutive description of plasticity at the single crystal scale – determined in general by the evolution of the crystal orientation and the plastic resistance on crystallographic slip systems – and implementation of these constitutive laws into full-field microstructural simulations using finite element, fast-Fourier (FEM, FFT) and other numerical methods [14,15]. They can thus describe the mechanical response of a polycrystal, considering the tensorial nature of plastic deformation [16], as well as its anisotropy [17]. In the context of precipitation, CP simulations have been successfully used to model the effect of precipitates on plastic anisotropy [18], ductility [19,20], localisation of deformation [21], or Bauschinger effect [10,22] in various materials. These models require as an input the particle size distribution in the precipitated microstructure.

The evolution of a precipitate population can be predicted as a function of time and temperature by kinetic models, based on nucleation and growth laws [23]. The precipitation rate is mainly controlled by the solute diffusion coefficient – that determines the solute transport velocity – and is driven by the supersaturation in the matrix (deviation from the equilibrium solute concentration). Numerous kinetic models have been developed to predict the precipitate characteristics in aluminium alloys [24–26] and a review of the modelling techniques is provided in [27]. When ageing is accompanied by deformation, the precipitation process can be significantly accelerated for reasons mentioned before.

Most of the modelling work focusing on age-hardened aluminium alloys address either the description of precipitate kinetics as a function of time and temperature [24–26], or the effect of precipitates on mechanical properties [18,20]. Some studies have combined mechanics and kinetics approaches to propose tools that (i) predict the precipitate distribution as a function of prior ageing time and temperature; (ii) use the calculated precipitate distribution as an input to predict the mechanical properties, usually considering it as constant over the deformation process [10,13,21,28]. Other models have focused on the effect of plasticity on diffusivity [2,8,29], on precipitate dissolution [26], on the precipitate nucleation rate [30], and the modelling of precipitate growth and coarsening kinetics in pre-aged aluminium alloys under deformation has been the focus of previous work [31]. However, there seems to be little modelling work addressing how plasticity and precipitation kinetics interact during deformation. A better comprehension of such interactions is of primary importance in understanding warm forming in age-hardened aluminium alloys. Indeed, warm deformation is necessarily accompanied by an evolution of the precipitate distribution and is affected by, as well as determining, this evolution.

The purpose of this work is to model the coupled effect of deformation and precipitation in age-hardened aluminium alloys at intermediate temperatures. This paper presents a CP model embedding a modified Kampman Wagner N-class (KWN) dynamic precipitation formulation described elsewhere [31], and is used to calculate the simultaneous evolution of local strain and precipitate distribution. The effect of precipitates and solid solution atoms on the critical stress for dislocation glide is calculated using the model of Deschamps et al. [13]. The model is used to explore the influence of dynamic precipitation on the development of strain heterogeneities, and to calculate how these strain heterogeneities lead to the development of heterogeneities in the precipitate distribution. The effect of dynamic precipitation on strength and uniform elongation is discussed, and a comparison is made between simulated precipitate distributions obtained after conventional heat treatment and after deformation. The differences expected between differently textured materials are predicted and discussed as well.

2. Model

2.1. Overview

The most important features of the full-field dynamic precipitation model used in this work are as follows:

- The crystal plasticity model uses the DAMASK framework [16] with a custom constitutive law including dynamic precipitation.
- A microstructure containing a pre-existing precipitate distribution is considered. The supersaturation is assumed to be sufficiently low for nucleation not to take place, so that only growth and coarsening are taken into account.
- Each voxel of the representative volume element (RVE) is characterised by its own precipitate distribution. Initially, the precipitate distribution is identical in all voxels and follows a log-normal distribution.
- At each voxel, a KWN model including dynamic precipitation [31] is run, so that at each time step the local precipitate distribution is updated. The local precipitate growth rate thus depends on the local deformation.
- The critical resolved shear stress for dislocation glide is calculated at each voxel and for all 12 face-centered cubic (FCC) slip systems, taking into account forest dislocations, solid solution hardening and precipitation hardening.
- For the sake of simplicity, the evolution of the dislocation contribution to the critical resolved shear stress is assumed to follow a phenomenological power-law. The formulation used for the hardening law supposes that the evolution rate of dislocation density is not affected by precipitate distribution. This hypothesis is generally considered as valid in the case where all precipitates are shearable [32], which is the case in the calculations made here, as will be shown later.
- Strain induced dissolution of shearable precipitates is assumed not to occur in the conditions studied here; this assumption will be discussed later.

The model is then used to simulate tensile tests for a single set of temperatures and strain rates (150°C and 10^{-4} s^{-1}). The influence of strain rate and temperature on dynamic precipitation has been discussed elsewhere [31]. These conditions were chosen since they were previously demonstrated to provide a strong dynamic effect whilst being relevant to industrial operations [31].

2.2. Crystal plasticity model

A crystal plasticity constitutive model is used and the plastic strain rate is given by [16]:

$$\mathbf{L}_{\mathrm{p}} = \sum_{\alpha=1}^{12} \dot{\gamma}^{\alpha} n^{\alpha} \otimes s^{\alpha} \tag{1}$$

where the indices α refer to the 12 FCC slip systems, defined by the slip plane normal n^α and the slip direction s^α, and $\dot{\gamma}^\alpha$ is the slip rate. The slip rates are given by an empirical power law [33]:

$$\dot{\gamma}^\alpha = \dot{\gamma}_0 \left(\frac{\tau^\alpha}{\tau^\alpha_*} \right)^n \tag{2}$$

where $\dot{\gamma}_0$ and n are constants, τ^α is the resolved shear stress on the slip system, and the slip resistance, τ^α_*, is given by [13]:

$$\tau^\alpha_* = \tau_s + \sqrt{(\tau_p)^2 + (\tau^\alpha_d)^2} \tag{3}$$

where τ_s, τ_p and τ^α_d are the contributions of the atoms in solid solution, of the reinforcing precipitates, and of the dislocations, respectively. τ_s is given by:

$$\tau_s = k_s \cdot c^{2/3} \tag{4}$$

where c is the concentration of solute elements in the matrix, which depends on the volume fraction of precipitates as described in Section 2.3, and k_s is an empirical constant [13]. The precipitation hardening contribution τ_p, is given by [13]:

$$\tau_p = \mu \sqrt{\frac{3 f_v}{2\pi}} \cdot \frac{k_p}{\bar{r} \cdot \sqrt{r_t}} \left(\int_0^{r_t} r \cdot \phi(r,t)\, \mathrm{d}\, r + \int_{r_t}^{\infty} r_t \cdot \phi(r,t)\, \mathrm{d}\, r \right)^{3/2} \tag{5}$$

where μ is the shear modulus, k_p is an empirical constant, r_t is the transition radius between shearing and Orowan looping [11], f_v and $\bar{r}$ are the volume fraction and mean radius of the precipitates, respectively, and $\phi(r,t)$ is the precipitate distribution function. The precipitate distribution $\phi(r,t)$ and precipitate volume fraction f_v change with deformation as detailed in Section 2.3. For the parameters (Section 3.1.3) and simulation conditions (Section 4.1.1) adopted in this work, and as will be seen later (for example in Fig. 11(b)), all particles in the distribution are systematically smaller than r_t, so that the second term in the integral in Eq. (5) vanishes, and the precipitation hardening contribution can be more simply expressed as:

$$\tau^\alpha_p = \mu \sqrt{\frac{3 f_v}{2\pi}} \cdot k_p \cdot \sqrt{\frac{\bar{r}}{r_t}} \tag{6}$$

In Eq. (3), τ^α_d is the resistance to slip due to forest dislocations, and the hardening rate is given by [33]:

$$\dot{\tau}^\alpha_d = h_0 \sum_{\beta=1}^{12} q_{\alpha\beta}\, \dot{\gamma}^\beta \left[1 - \frac{\tau^\beta_d}{\tau_\infty} \right]^a, \tag{7}$$

where h_0, τ_∞ and a are hardening parameters, and $q_{\alpha\beta}$ is the latent hardening between the slip systems α and β, equal to 1 for coplanar slip systems and 1.4 otherwise [33].

2.3. Dynamic precipitation model

2.3.1. Precipitation kinetics

The alloy considered here is A7075, with composition 5.6% Zn, 2.5% Mg, 1.6% Cu (weight percent) and Al balance. The precipitates are assumed to be metastable $\eta\prime$, with stoichiometry $Mg_5Zn_7Al_6$ [31]. A pre-existing precipitated microstructure is considered, and its initial distribution is assumed to follow a log-normal law, characterised by an initial precipitate mean radius r_0, an initial precipitate volume fraction f^0_v, and a dispersion parameter s [31,34].

At moderate temperatures (100 to 200 °C), dynamic precipitation is mainly controlled by the production and annihilation of excess vacancies [8]. In the present work, a KWN framework – extended to account for the effect of deformation – is used, enabling prediction of the evolution of the precipitate distribution $\phi(r,t)$ in each material point of the CP simulation domain. This model has been described elsewhere [31], and only the essential features are summarised here.

Following the KWN method, the precipitate distribution function $\phi(r,t)$ is discretised in N classes of width Δr characterised by their size r_i. At each time step, the new precipitate size distribution is determined by calculating the growth rate $\left[\frac{dr}{dt}\right]_i$ in each bin of the size distribution, and reallocating the particles in the neighbouring bins as explained in [35]. The growth rate is considered to be controlled by the diffusion of Mg atoms, which are the slowest diffusers in this alloy, and is calculated as:

$$\left[\frac{dr}{dt}\right]_i = \frac{D_{\mathrm{eff}}}{r_i} \cdot \frac{\bar{x}_{\mathrm{Mg}} - x^{r_i}_{\mathrm{Mg}}}{x^{\mathrm{pr}}_{\mathrm{Mg}} - x^{r_i}_{\mathrm{Mg}}} \tag{8}$$

where D_{eff} is the effective diffusion coefficient of Mg, enhanced by deformation as detailed in Section 2.3.2; $x^{\mathrm{pr}}_{\mathrm{Mg}}$ is the concentration of Mg in the precipitate, $\bar{x}_{\mathrm{Mg}}$ is the average concentration of Mg remaining in the matrix, and $x^{r_i}_{\mathrm{Mg}}$ is the equilibrium concentration at the interface between the matrix and a precipitate of radius r_i. The latter takes into account the Gibbs–Thompson effect and is calculated as the intersection between the stoichometric line and the solvus line, which, for a precipitate of composition $Mg_5Zn_7Al_6$ and size r_i are respectively defined by Eq. (9) and Eq. (10)

$$7 \cdot (x^0_{\mathrm{Mg}} - x^{r_i}_{\mathrm{Mg}}) = 5 \cdot (x^0_{\mathrm{Zn}} - x^{r_i}_{\mathrm{Zn}}) \tag{9}$$

$$K^\infty(T) \exp\left(\frac{2\gamma v^{pr}_{\mathrm{at}}}{r_i kT} \cdot (5+7+6) \right) = (x^{r_i}_{\mathrm{Mg}})^5 \cdot (x^{r_i}_{\mathrm{Zn}})^7 \tag{10}$$

where γ is the interfacial energy, v^{pr}_{at} is the atomic volume of the precipitating phase, and $K^\infty(T)$ is the solubility product at the temperature T, calculated as:

$$K^\infty(T) = \exp\left(\frac{\Delta S}{R} - \frac{\Delta H}{RT} \right) \tag{11}$$

where ΔS and ΔH are the entropy and enthalpy of formation of precipitates, respectively, and R is the gas constant.

2.3.2. Deformation induced enhanced diffusivity

The diffusivity of solute elements depends on the concentration of excess vacancies through:

$$D_{\mathrm{eff}} = D_{\mathrm{th}} \left(1 + \frac{c_{\mathrm{ex}}}{c_{\mathrm{th}}} \right) \tag{12}$$

where D_{th} is the diffusion coefficient without deformation, calculated in the usual way with the prefactor D_0 and the activation energy for solute migration Q; c_{ex} is the number of excess vacancies, calculated as outlined below; and c_{th} is the equilibrium concentration of thermal vacancies, calculated as $c_{\mathrm{th}} = 23 \exp(\frac{-Q_f}{kT})$ [36], where Q_f is the vacancy formation energy.

The rate of generation and annihilation of excess vacancies due to plastic deformation is given by

$$\dot{c}_{\mathrm{ex}} = \chi \frac{\Omega}{Q_f} \sum_{\alpha=1}^{N} \dot{\gamma}^\alpha \tau^\alpha + 0.5 \cdot \exp(-\frac{Q_j}{kT}) \frac{\Omega}{4b^3} \sum \dot{\gamma} - \frac{D_{\mathrm{V}}}{\kappa^2 L^2} c_{\mathrm{ex}} \tag{13}$$

where, χ is the fraction of plastic work converted into vacancies, Ω is the atomic volume of the alloy, Q_f and Q_j are the vacancy and jog formation energy, respectively, κ is a constant related to dislocation arrangement, and D_v is the diffusion coefficient of vacancies, equal to $D^v_0 \exp(-\frac{Q_m}{kT})$, where Q_m is the activation energy for vacancy migration. L is the average spacing between vacancy sinks. Assuming that vacancies annihilate at the closest dislocation, the vacancy sink spacing is calculated as $1/\sqrt{\rho}$, where ρ is the dislocation density, which is calculated using the Taylor relation as:

$$\rho = \left[\frac{\max_{\alpha=1..N}(\tau^\alpha_d)}{\beta \mu b} \right]^2 \tag{14}$$

where β is a constant usually taken as 0.27 [13] and b is the burgers vector. The dislocation density is therefore related to the plastic shear rate as stated in Eq. (7).

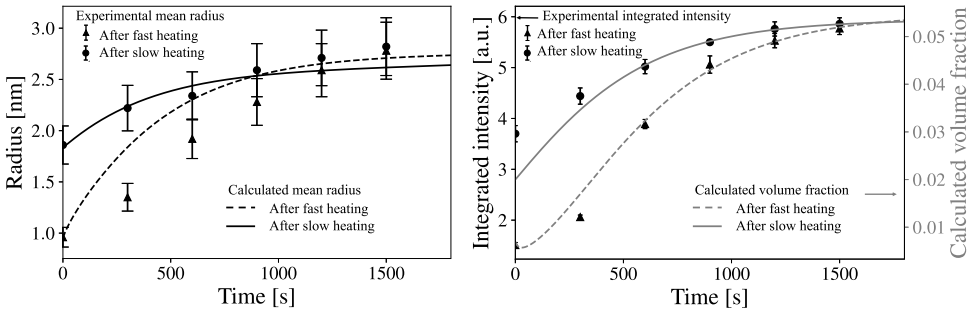

Fig. 1. Comparison of (a) the calculated mean radius and measured Guinier radius; (b) the experimental integrated density and the calculated volume fraction. The experiments are made at 185°C after slow and fast heating, respectively, to 185°C, which leads to different distributions at the beginning of the ageing treatment.

Table 1
Model inputs for static ageing.

Symbol	Input	Fast heating	Slow heating
T	Temperature	185 °C	185 °C
r_0	Initial mean radius	0.96 nm	1.86 nm
v_f^0	Initial volume fraction	0.007	0.02
s	Dispersion parameter	0.2	0.2

3. Identification of model parameters

The crystal plasticity model including dynamic precipitation contains several parameters that need to be calibrated to experimental data. The model parameters can be separated in three groups, namely the parameters related to precipitation kinetics, the parameters related to the excess vacancy model, and the parameters for the constitutive law in the CP simulations.

3.1. Model parameters

3.1.1. Precipitation kinetics parameters

The parameters related to precipitation kinetics were identified using SAXS experiments – presented elsewhere [37] – measured during ageing at 185 °C without any deformation, where the temperature is sufficiently high to allow for significant precipitate evolution in a short amount of time. The precipitate distribution evolution was measured during isothermal holding, after fast and slow heating from room temperature, respectively. This produces two different initial precipitate distributions. The input parameters of the model corresponding to these experiments are presented in

Table 1.

The kinetics parameters adopted here are shown in Table 2. The enthalpy and entropy of precipitation for η' in 7075 were obtained from Thermocalc software and TCAL8 database, similarly as in [31] and the interfacial energy is adjusted here so as to reach acceptable agreement between calculations and measurements.

Fig. 1(a) shows the comparison between the calculated and experimental precipitate mean radius, and Fig. 1(b) shows the calculated volume fraction, along with the measured integrated density, which is expected to be proportional to the volume fraction. An experimental error of 10% is considered in Fig. 1(a), corresponding to the expected maximal difference between the Guinier radius and the mean radius for the distribution considered here [34,38].

3.1.2. Excess vacancy model parameters

The parameters for the excess vacancy model have been determined and discussed for another alloy from the 7xxx series (7449 alloy) in a previous study [31], and the same set of parameters is adopted here for the sake of simplicity (see Table 3).

3.1.3. Crystal plasticity model parameters

The crystal plasticity model parameters were fitted to a set of two experimental stress–strain curves measured at 150 °C with strain rates of 0.1 s^{-1} and 1 s^{-1}, respectively, under uniaxial tension [37]. The preexisting precipitate distribution for this set of experiments was the same as the one described for fast heating in Table 1. To fit the experimental results, a RVE containing 159 grains with a resolution of 32 × 32 × 32 elements was used. The orientations of the grains were sampled using MTEX to reproduce an experimental EBSD map of the cold-rolled material [40]. The CP parameters were then fitted to reach good agreement between calculations and experiments. The adopted parameters are shown in Table 4, together with reference values from the literature.

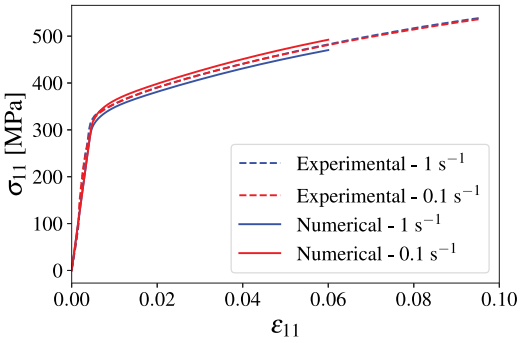

Fig. 2. Simulated and calculated stress strain curve during uniaxial tensile test at 150 °C.

The simulated and experimental stress strain curves obtained with the calibrated CP model are compared in Fig. 2. In all this work, σ_{11} and ϵ_{11} refer to the Cauchy stress and true strain, respectively, in the tensile direction. The presented values of σ_{11} and ϵ_{11} are averaged over the volume of the RVE, unless otherwise stated.

4. Application and discussion

4.1. Effect of dynamic precipitation on mechanical properties

4.1.1. Simulation set up

A representative microstructure of the test sample was generated with a set of 27 equiaxed grains randomly orientated in a 32 × 32 × 32 box, with periodic boundary conditions. The representative volume element (RVE) is shown in Fig. 3.

To illustrate how dynamic precipitation affects mechanical properties, a tensile test was simulated both by considering a precipitate distribution that changes during the deformation - considering dynamic precipitation - and for a precipitate distribution kept constant during the deformation - ignoring dynamic precipitation. For both cases, the initial precipitate distribution is the same as in Section 3.1.3 and all voxels display the same initial particle size distribution, shown in Fig. 3(b).

The model is demonstrated with a tensile test simulated at 150°C with a strain rate of 10^{-4} s^{-1}. The choice of this strain rate and

Table 2
Kinetics parameters.

Symbol	Parameter	Value	Literature
D_0	Pre-factor diffusion coefficient	1×10^{-5} $m^2.s^{-1}$	(0.63 to 12)×10^{-5} $m^2.s^{-1}$ [39]
Q	Migration energy	123.5 $kJ.mol^{-1}$	112.1 to 161.1 $kJ.mol^{-1}$ [39]
γ	Interfacial energy	265 $mJ.m^{-2}$	50 to 400 $mJ.m^{-2}$ [31]
ΔH	Enthalpy of precipitation	290 $kJ.mol^{-1}$	–
ΔS	Entropy of precipitation	62 $J.mol^{-1}$	–

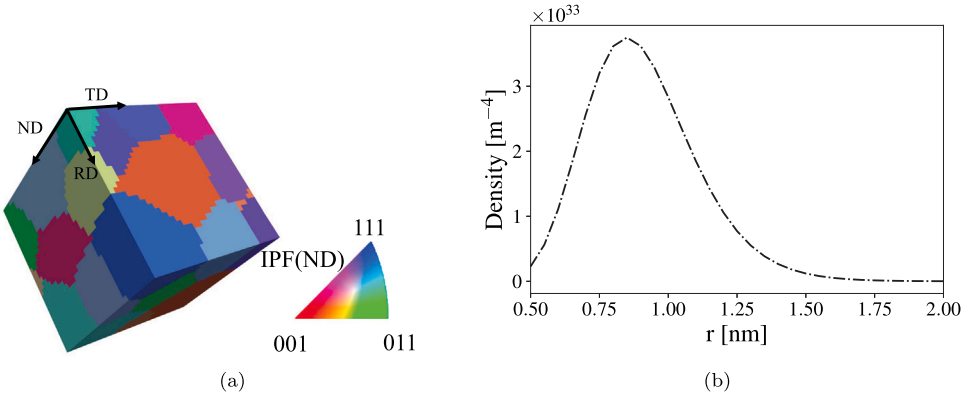

Fig. 3. (a) Inverse pole figure (IPF) map of the simulated RVE with respect to the normal direction (ND). RD and TD refer respectively to the rolling and transverse directions. (b) Simulated initial particle size distribution.

Table 3
Parameters for deformation induced excess vacancy model [31].

Symbol	Parameter	Value
D_0^v	Prefactor for vacancy diffusion	$1.49 \times 10^{-5} m^2.s^{-1}$
Q_m	Vacancy migration energy	0.93 eV
Q_f	Vacancy formation energy	0.52 eV
Q_j	Jog formation energy	0.3 eV
κ	Dislocation arrangement constant	10
χ	Mechanical vacancy production term	0.035

temperature is guided by calculations made with a single point dynamic precipitation model [31], which suggested that deformation significantly accelerates precipitation kinetics for this set of conditions.

4.1.2. Stress–strain response

Dynamic precipitation results in an increase in the tensile stress of 60 MPa during the deformation, as can be seen in Fig. 4(a). This increase compared to the situation where the precipitate distribution is considered as constant (dotted line) - is due to the increase in the precipitate volume fraction and mean radius, shown in Fig. 4(b). This can be illustrated by plotting the average contributions of each hardening effect to the stress (Eq. (3)), as shown in Fig. 5, where $\tau_d^{\max}$ is the highest shear stress on all the slip systems (maximum value of τ_d^{α}) averaged on all voxels. It can first be seen in the figure that the calculated contribution of the dislocations $\tau_d^{\max}$ is similar with and without dynamic precipitation at 0.1 MPa, which is a consequence of the fact that shearable precipitates are assumed not to affect dislocation storage and recovery [32]. In the case where dynamic precipitation is considered, the solid solution contribution τ_s decreases from 91 to 47 MPa during the deformation as precipitates grow and deplete the matrix in solute, but this weakening effect is overcome by the concomitant increase in the precipitation hardening effect (τ_p). As a result, dynamic precipitation causes a net increase in the flow stress, as expected from precipitation hardening models [13].

4.1.3. Work hardening

The simulated macroscopic strain hardening rate can be seen in Fig. 6. The figure shows that dynamic precipitation induces a higher work hardening rate than if no dynamic precipitation occurs, until the hardening potential associated with the growth of precipitates is almost exhausted. This can be illustrated for example in Fig. 5, where the rate of increase in the precipitation hardening contribution reduces as strain increases. After sufficient deformation (around 0.13 in Fig. 6), the work hardening rate becomes similar to the case without any dynamic precipitation.

4.1.4. Uniform elongation

The crystal plasticity simulations can be used to determine the influence of dynamic precipitation on uniform elongation. A simple and frequently used criterion to determine when strain localisation takes place is the so-called “Considère criterion” [43], that states that plastic instability occurs when the flow stress becomes larger than the work hardening rate. Fig. 7 shows the calculated work hardening rate and flow stress in the first grain expected to undergo strain localisation, thus being responsible for the end of the uniform deformation. The figure shows that the uniform elongation is predicted to be higher with dynamic precipitation.

These results demonstrate that dynamic precipitation has potential to lead to an improved strength and ductility, compared to the situation where the precipitation distribution remains constant during deformation. This is the case, even though the precipitates remain fully in the shearable size regime.

4.1.5. Local stress and strain heterogeneities

As deformation takes place, strain and stress heterogeneities develop. Since dynamic precipitation is more significant in regions where the local strain is greater, it is of interest to calculate how dynamic precipitation affects the development of strain and stress heterogeneities. For this purpose, Fig. 8 shows the calculated von Mises stress and strain distributions with and without dynamic precipitation, for a macroscopic tensile strain of 0.18. The results shown in Fig. 8(a) suggest that dynamic precipitation does not significantly affect the strain distribution. The von Mises stress distribution is shown in Fig. 8(b). Although the average von Mises stress is higher with dynamic precipitation then without it – which is due to a higher volume fraction of precipitates as previously discussed – it can also be seen that dynamic precipitation does not significantly affect the heterogeneities. Indeed the stress distributions with and without dynamic precipitation look alike except for the shift in the average value. It can thus be concluded that for the

Table 4
CP parameters.

Symbol	Parameter	Value	Literature
τ_d^0	Initial CRSS for dislocation glide at 150 °C	7.8 MPa	[41]
τ_∞	Saturation CRSS for dislocation glide	163 MPa	118 MPa [16]
$\dot{\gamma}_0$	Slip rate constant	1×10^{-3} s^{-1}	[16]
h_0	Hardening parameter	763 MPa	2.48 GPa [16]
a	Hardening parameter	2.25	2 [16]
n	Slip rate law exponent	50	[16]
k_p	Precipitation hardening constant	0.035	0.07 [13]
k_s	Solid solution hardening constant	683 MPa	840 MPa [13]
r_t	Transition radius shearing-looping	3.3 nm	[42]

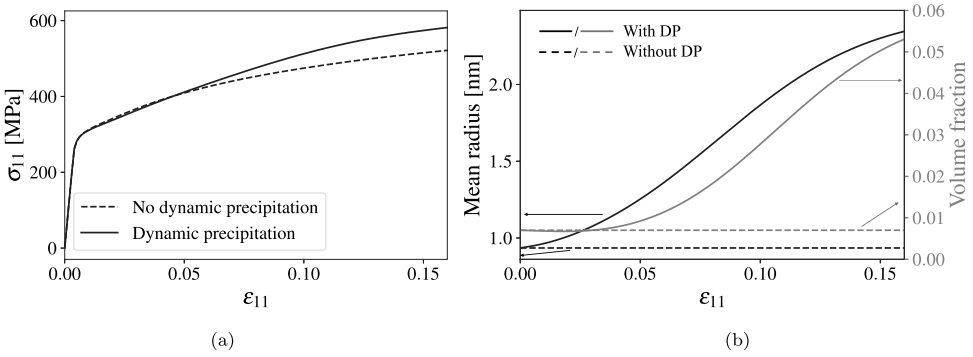

Fig. 4. Evolution of (a) stress and strain along the tensile direction (b) total precipitate volume fraction and mean radius during deformation (150 °C - 1×10^{-4} s^{-1}). The grey curves refer to the volume fraction and right hand side axis while the black curves refer to the mean radius and left hand side axis. For (a) and (b), the plain lines show the results of simulations where dynamic precipitation is considered, while the dotted lines show the results of simulations where dynamic precipitation is ignored, i.e. where the precipitate distribution is kept constant during the simulation.

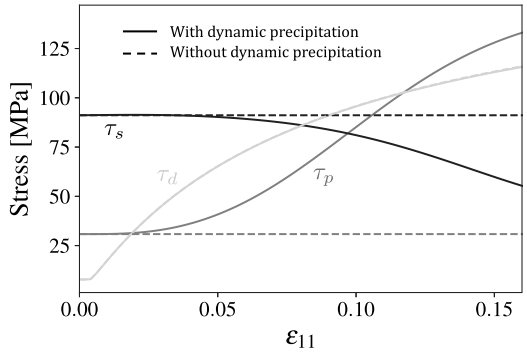

Fig. 5. Calculated average contribution of dislocation density (τ_d), solid solution hardening (τ_s) and precipitation hardening (τ_p) to the stress along the tensile direction, with and without considering dynamic precipitation.

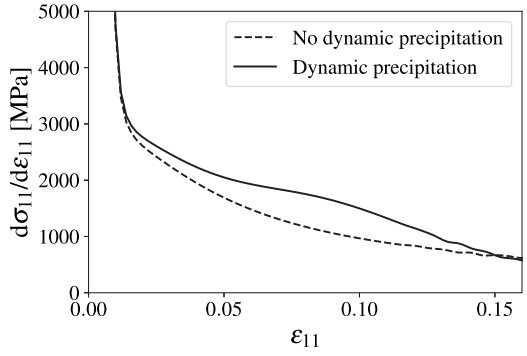

Fig. 6. Calculated macroscopic strain hardening in the tensile direction calculated with and without dynamic precipitation (150 °C - 1×10^{-4} s^{-1}).

conditions investigated here, dynamic precipitation seems to increase the flow stress of the material without strongly affecting the stress and strain heterogeneity development. Such behaviour appears consistent

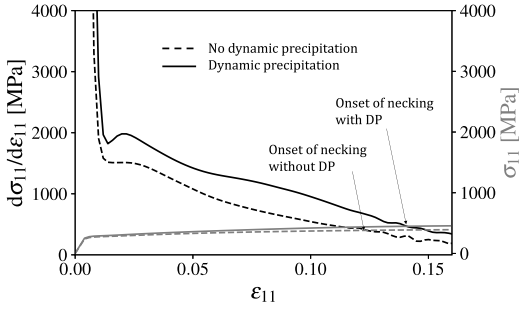

Fig. 7. Work hardening rate and tensile stress in the elongation direction calculated as a function of the tensile strain in the first grain expected to display strain localisation, calculated both considering and ignoring dynamic precipitation (150 °C - 1×10^{-4} s^{-1}). According to the Considère criterion, the intersection between the stress curve and the work hardening rate curve corresponds to the onset of strain localisation.

with what has been observed during dynamic precipitation of GP zones in an Al–Cu alloy [44]. It should be noted that this conclusion is valid as long as the dislocation hardening law is not strongly affected by the changes in precipitate distribution, which should be the case for shearable precipitates that do not undergo significant strain-induced dissolution. This assumption is discussed below.

4.1.6. Discussion on deformation-induced dissolution of shearable precipitates

During plastic deformation, dislocations shear the particles, which can cause them to dissolve [45]. This may promote local softening and affect the development of strain heterogeneities. One of the limitations of the present model is that, as previously mentioned, this effect is ignored. However, comparison with experiments from the literature indicate that shearing induced particle dissolution may be ignored for the conditions considered here. Indeed, according to the model proposed by Hutchinson et al. [45], strain-induced dissolution of precipitates is promoted by slow solute diffusion and by deformation

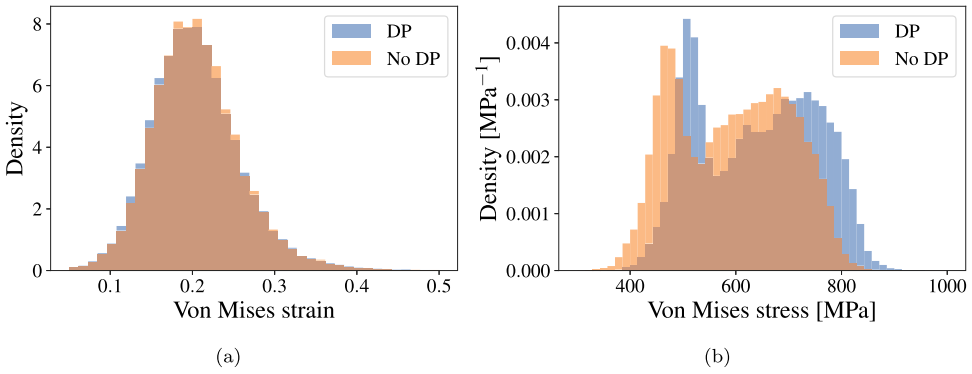

Fig. 8. Von Mises strain (a) and stress (b) after 0.18 deformation (150 °C - 1×10^{-4} s^{-1}), considering and ignoring dynamic precipitation.

at fast strain rate and up to high strain. In experimental work from the literature, no strain-induced dissolution was observed in an Al–Cu–Mg alloy deformed at room temperature with a strain rate of 1.5 s^{-1} up to 40% deformation [45]. Since, compared to the aforementioned experimental work, the model presented here is applied to higher temperature (resulting in faster diffusion), and to deformation at both lower strain rate and lower strain, it can be confidently assumed that strain-induced dissolution does not take place either for the conditions studied here. Strain-induced dissolution may however need to be incorporated in the model in order to apply it to high strain rate and low temperature.

4.2. Precipitate distribution heterogeneities

Since the precipitate growth rate at a specific point in the microstructure depends on the local stress, strain, and strain rate, the strain heterogeneities that develop during the deformation result in a spatial variation in the precipitate evolution The precipitate distribution then determines the local micro-mechanical properties, and is therefore important to quantify how deformation at intermediate temperature affects the final precipitate distribution.

4.2.1. Development of precipitate heterogeneities

The spatial evolution of the precipitate mean radius distribution during deformation, for an RVE with a random texture described previously, is shown in Fig. 9, along with the evolution of the von Mises strain. In the initial state, the precipitate distribution is identical in all voxels. As deformation takes place, strain heterogeneities appear, and Fig. 9 shows how the regions undergoing higher strain also experience greater precipitate growth. It can be noted, that, although the spatial distribution of precipitate radius correlates with the level of strain experienced, the heterogeneities in the spatial precipitate radius distribution appear qualitatively weak compared to the developed strain heterogeneities. This seems to be consistent with experimental results, where, despite deformation, precipitate distribution was observed to be relatively homogeneous [5,44,46,47]. It may be also be noted that strong heterogeneity develops at the onset of plasticity, and then homogenises as deformation carries on. The reasons for this will be further discussed below.

4.2.2. Differences of growth rate inside and between grains

The spatial heterogeneities in the precipitate mean radius are shown in more detail for the greatest level of strain in Fig. 10(a). The figure shows the spatial distribution of the von Mises strain and of the mean radius in a slice of the RVE containing both the grain of the RVE experiencing the fastest growth - labelled G_f in the figure - and the grain experiencing the slowest growth - labelled G_s in the figure. Fig. 10(a) shows that G_s experiences a lower average strain compared to the neighbouring grains, and contains a region where the von Mises strain is as low as 0.3% for a macroscopic strain of 18%. As a result, the precipitate growth in this under-strained region is lower than in the rest of the RVE, with some voxels containing precipitates of 1.7 nm radius, significantly smaller than the precipitates in the most highly strained regions, that reach a radius of 2.6 nm. In the grain experiencing the fastest precipitate growth (G_f), the von Mises strain is predicted to be both more homogeneous and higher than in the neighbouring grains. This results in a rather homogeneous distribution of precipitates inside the grain, with precipitates predicted to be slightly larger than in the surrounding grains.

In order to measure the differences in precipitate growth both inside and between the different grains, Fig. 10(b) shows the evolution of the mean radius in the previously defined G_s and G_f grains as a function of strain. The figure shows that although there is a difference in growth rate up to the maximum strain used here (18%), it is not sufficient to produce a large difference in the mean precipitate radius. The halos surrounding the curves represent the in-grain differences in local mean precipitate radius for each grain – 90% of the precipitates in the grain have radius inside this area – and demonstrate that the variation within a given grain is of the same order of magnitude than the variation between grains for the case studied here. Indeed, there is overlap between the mean radius inside the two grains, with the largest precipitates in G_s having higher radius than the smallest precipitates in G_f. It can be concluded that, compared to the precipitate growth experienced by the RVE during deformation, both the variations of growth inside the grains and between the grains are small. This demonstrates that for the conditions studied here, dynamic precipitation is spatially heterogeneous, but that this heterogeneity is rather weak. Reasons for this mild heterogeneity will be discussed later, along with the influence of grain orientation.

4.2.3. Comparison between static and dynamic precipitation

Once a part has been shaped, its mechanical properties depend on the precipitate distribution. It is therefore useful to compare the precipitate distribution resulting from dynamic precipitation to that obtained after conventional static heat treatment. For this purpose, the evolution of the precipitate distribution without any deformation at 150 °C was calculated, using the same initial distribution as the one described in Section 4.1.1. The calculated evolution of the precipitate volume fraction is shown in Fig. 11(a), along with the evolution of the volume fraction under deformation. As can be seen in Fig. 11(a), deformation is expected to result in a significant acceleration of the precipitation for this strain rate and temperature regime. In order to measure the effect of deformation on the final precipitate distribution, the distribution obtained after an arbitrary reference time t_2 =10 000 s of static heat treatment at 150 °C was compared to the distribution obtained after deformation for a duration t_1, which is the time necessary to reach the same volume fraction as after t_2 in static conditions (Fig. 11(a)). The distributions obtained after static and dynamic heat treatment at 150 °C are shown in Fig. 11(b).

First of all, it can be seen from Fig. 11(a) that the precipitate growth is around an order of magnitude faster under deformation than

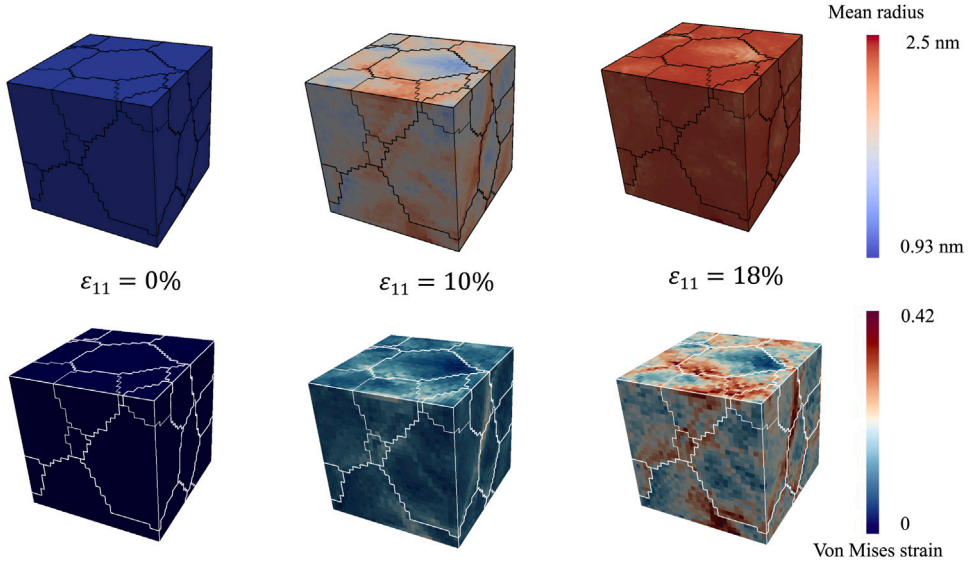

Fig. 9. Predicted evolution of local mean precipitate radius (top) and von Mises strain (bottom) in an RVE with random texture (150 °C - 1×10^{-4} s^{-1}). The grain boundaries are indicated by black (top figures) or white (bottom figures) lines.

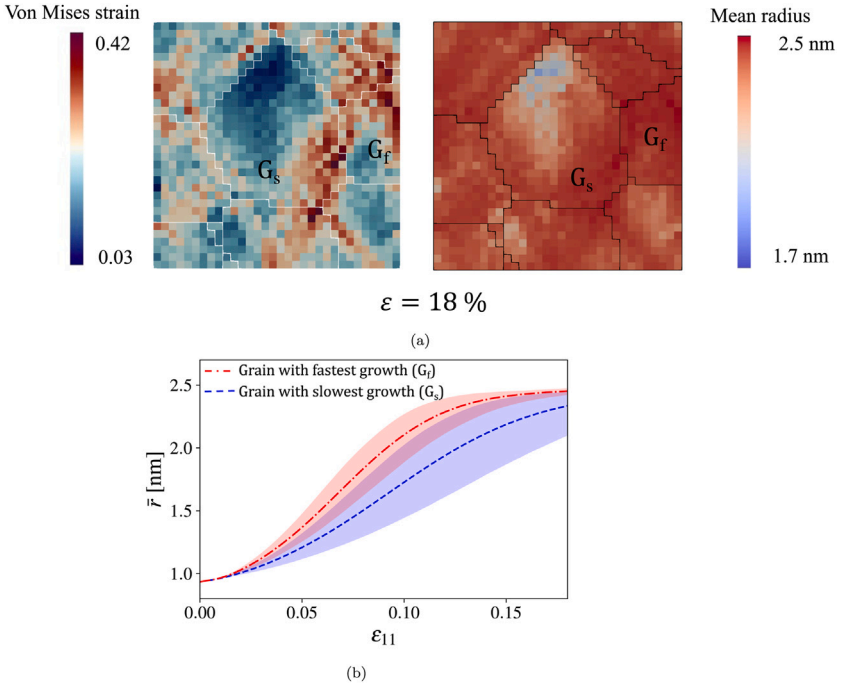

Fig. 10. (a) Predicted evolution of von Mises strain and local mean precipitate radius in a slice of the RVE with random texture after 18% deformation (150°C - 1×10^{-4} s^{-1}). The grain boundaries are indicated by black or white lines. G_s is the grain of the RVE displaying the slowest precipitate growth and G_f is the grain displaying the fastest precipitate growth. (b) Mean radius evolution for grains with minimum (G_s) and maximum (G_f) growth rate (150 °C - 1×10^{-4} s^{-1}). The lines show the evolution of the average value of the mean radius in the grain while the halos around the curve shows a 80% confidence interval for the mean radius inside the grain.

under static conditions ($t_1 = t_2/8.8$). Further, Fig. 11(b) shows that, for equal precipitate volume fractions, the distribution after deformation is not the same as that following static heat treatment. The deformed particle size distribution has a wider distribution, which is a result of the spatially heterogeneous nature of dynamic precipitate evolution, as already demonstrated. Such wider distribution for dynamically aged material compared to statically aged material has been experimentally reported in an Al alloy [48].

4.3. Influence of texture

4.3.1. Simulation set-up

In order to quantitatively evaluate the effect of texture on dynamic precipitation, the simulation described in Section 4.1.1 was reproduced with an RVE displaying a more realistic texture. This RVE was obtained by sampling an experimental EBSD map of a cold-rolled A7075 sheet [40] with MTEX software, using 32 × 32 × 32 resolution and

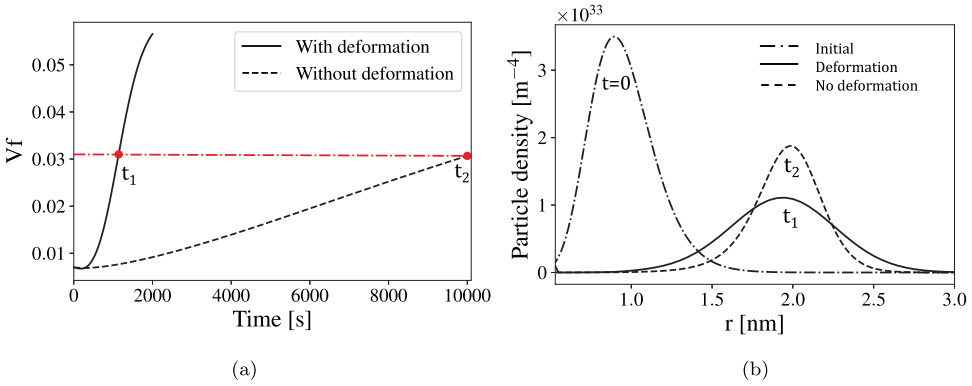

Fig. 11. Calculated evolution of the precipitate volume fraction with deformation (150 °C - 1×10^{-4} s^{-1}) and during static ageing. (b) Predicted particle size distribution after deformation for a duration t_1 and after static ageing for a duration t_2. The durations t_1 and t_2 are shown in (a).

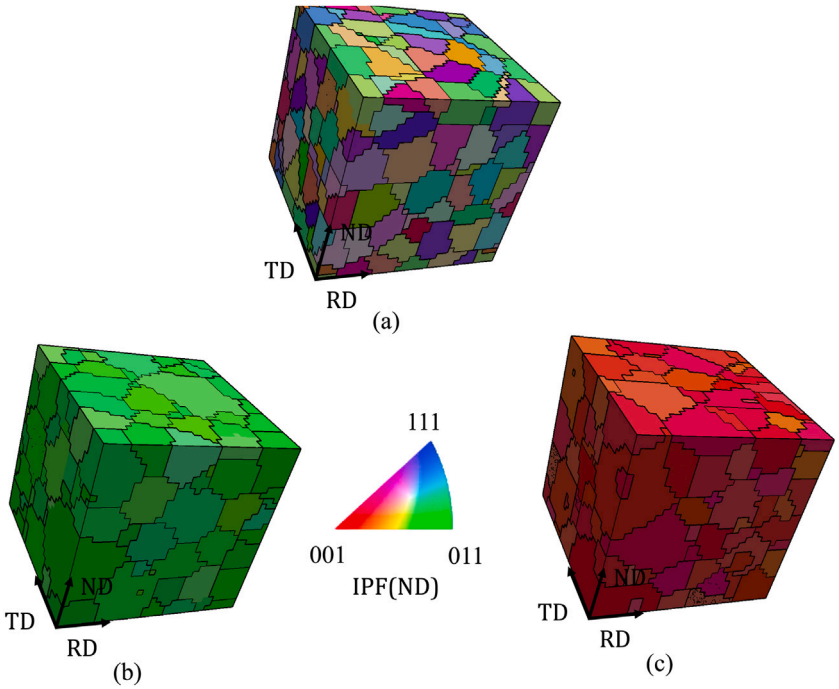

Fig. 12. Inverse pole figures with respect to the normal direction (ND) for the simulated microstructures reproducing (a) cold-rolled texture (sampled from EBSD map) (b) brass texture (c) cube texture. RD and TD refer respectively to the rolling and transverse directions.

159 grains, similarly to what was done to calibrate the model in Section 3.1.3. Additionally, DREAM3D software was used to create microstructures with near ideal artificially generated cube ($\{001\}\langle100\rangle$) texture with 180 grains and brass texture $\{110\}\langle112\rangle$ with 178 grains, respectively, using a weight value of 500 000 and sigma value of 2 [49]. These ideal textures develop different levels of strain heterogeneity (as demonstrated later) and were studied to help quantify the maximum effect texture may play on dynamic precipitation in aluminium alloys. The inverse pole figures (IPF) maps of the generated microstructures are displayed in Fig. 12. The Tensile tests were simulated as described in Section 4.1.1, at 150°C and with a strain rate of 1×10^{-4} s^{-1}, with the tensile axis aligned with the rolling direction (RD in Fig. 12).

4.3.2. Correlation between macro-mechanical taylor factor and precipitate localisation

In the case of the cold-rolled microstructure shown in Fig. 12(a), the influence of the local crystal orientation on precipitate evolution can be evaluated using the so-called "macro-mechanical Taylor factor" M^{macro}, defined by Raabe and co-authors as [50]:

$$M^{\text{macro}} = \sum_{\alpha=1}^{12} \gamma^{\alpha} / \epsilon_{\text{vM}}^{\text{global}} \tag{15}$$

where $\epsilon_{\text{vM}}^{\text{global}}$ is the externally exerted von Mises strain. To see how the individual orientation of the crystals – or kinematic hardness – affects precipitation evolution, the macro-mechanical Taylor factor, as well as the local volume fraction and local time-derivative of the volume fraction were calculated in each voxel of the simulated microstructure and for all time steps. The correlation coefficient[2] was then calculated between M^{macro} and v_f, as well as between M^{macro} and dv_f/dt. The results are shown in Fig. 13(a).

It can be seen from Fig. 13(a) that, at the beginning of plastic deformation, and up to a strain of about 10%, the local precipitate

[2] defined as the non-diagonal term of the covariance matrix between the two quantities.

volume fraction is strongly correlated with M^{macro}, and that the grains with maximal macro-mechanical Taylor factor experience the fastest precipitate growth. This is because, for a given level of overall strain, regions with high macro-mechanical Taylor factor have undergone more slip activity; these are therefore the regions where the highest amount of excess vacancies is produced. This can be qualitatively seen on the left hand side of Fig. 13(b), where the spatial distributions of M^{macro} and v_f are displayed for 5% plastic deformation. The figure shows that the regions displaying a high M^{macro} exhibit high precipitate volume fraction. As the deformation proceeds, however, the correlation coefficient between local volume fraction and M^{macro} decreases, and it can indeed be seen on the right hand side of Fig. 13(b) that for 19% of macroscopic deformation, the correspondence between regions of high M^{macro} and regions with high precipitate volume fraction is less apparent. The correlation between M^{macro} and v_f thus confirms that localisation of plastic deformation results in localisation of precipitates at the onset of plastic deformation, but that this effect reduces with further plastic deformation, as already noted above.

The decreasing influence of plastic localisation on precipitate localisation as the level of deformation increases can be interpreted by observing the correlation factor between the time derivative of the volume fraction (precipitate growth rate dv_f/dt) and M^{macro}, as shown in Fig. 13(a). At the onset of plastic deformation, the correlation factor equals unity, which means, that – as already mentioned – grains with maximal macro-mechanical Taylor factor experience fastest precipitate growth. However, for higher levels of deformation ($\epsilon > 11\%$), the correlation becomes negative, which means that at that stage, the grains exhibiting the fastest precipitate growth are grains with low value of M^{macro}. This is due to the fact that, since regions with high M^{macro} experience early and fast precipitation, they quickly reach solute equilibrium, after which precipitation becomes faster in regions with low M^{macro}, that have not yet experienced as much precipitation. The result of this process is that, after a certain level of deformation, precipitation appears relatively homogeneous in the microstructure, despite spatial heterogeneity in plastic deformation.

It should be noted that this weak influence of crystal orientation on precipitate localisation after a certain level of deformation may be attributed to the fact that Al is mildly plastically anisotropic, thus resulting in relatively homogeneous repartition of the plastic work. This homogeneous repartition results in rather homogeneous precipitation kinetics. However, the results might be quite different in more plastically anisotropic systems, such as hexagonal-closed-packed metals, e.g. in magnesium alloys.

4.3.3. *Influence of texture on precipitate size distribution*

The limited influence of local grain orientation on dynamic precipitation discussed in Section 4.3.2 can be emphasised by plotting the precipitate size distribution after deformation in the three simulated microstructures of Fig. 12 that represent, respectively, a realistic cold-rolled texture and two model cases with a cube texture (exaggerated case of what may be obtained after recrystallisation) and brass texture (exaggerated case of what may be obtained after heavy deformation). As can be seen in Fig. 14, despite significant differences between the strain distributions for the different simulated textures, the differences in the precipitate distribution obtained after deformation are small. This confirms that dynamic precipitation is only weakly affected by overall texture, at least in pre-aged microstructure where nucleation does not take place.

5. Conclusions

This work presents a crystal plasticity model including the effect of dynamic precipitation. The model has been applied to the case of warm deformation of AA7075 aluminium alloy with a pre-aged microstructure in which all precipitates are shearable. This is the most relevant condition for industrial warm forming of age hardening aluminium

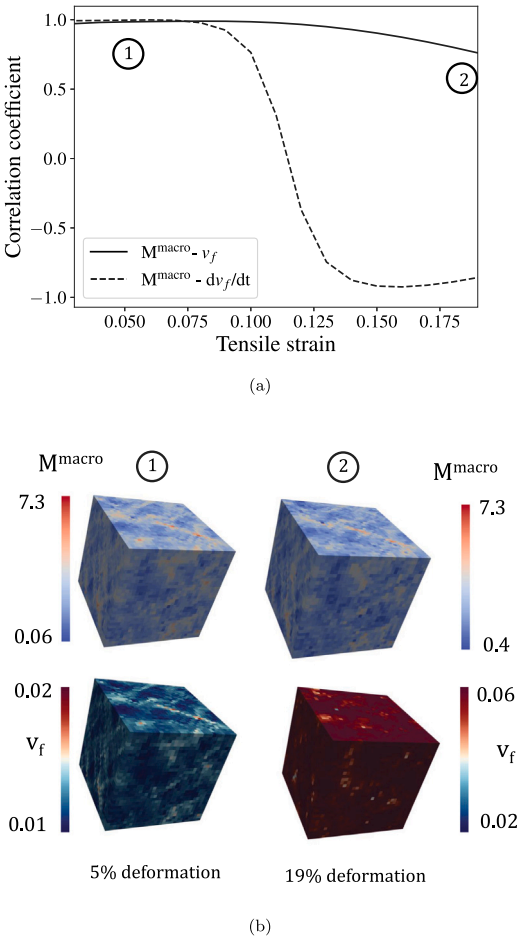

Fig. 13. (a) Correlation coefficient between precipitate volume fraction and M^{macro}, and between the time derivative of the volume fraction and M^{macro}, as a function of external tensile strain. For each level of strain, the correlation coefficient is calculated using the 32^3 voxels of the simulated microstructure. (b) spatial distribution of M^{macro} and v_f in the microstructure for 5% and 19% external deformation.

alloys. The model takes into account the strong coupling between precipitation and deformation; namely, the accelerating effect of deformation on precipitate growth and coarsening, and the strengthening effect of the evolving precipitates on deformation. The model allows exploration of the role of dynamic precipitation on the microstructural evolution, mechanical properties, and micro-scale heterogeneities. The following conclusions may be drawn from this work:

- Dynamic precipitation is predicted to result in both an increase in flow stress and uniform elongation compared to a situation where the precipitate distribution is constant during deformation. For the case considered here, the calculated gain yields 2% of uniform elongation and 50 MPa of flow stress.
- Dynamic precipitation, in the case of a pre-aged microstructure at least, is not expected to play a major role in the development of plastic strain heterogeneities.
- The precipitate distribution obtained following dynamic ageing is predicted to be more heterogeneous than that obtained after static ageing, but the precipitate growth localisation is expected to be modest compared to the strain localisation.
- Texture only weakly affects the precipitate distribution obtained following dynamic ageing. While, during the first stages of plastic deformation, precipitates might grow preferentially in kinematically hard grains, this effect softens for higher levels of deformation (above 10% in the present case).

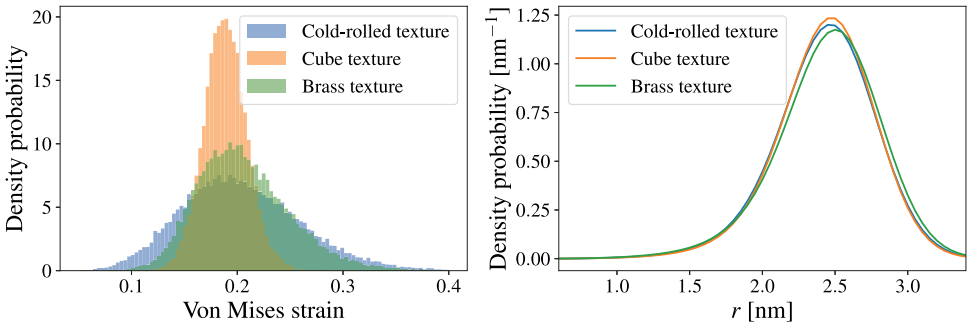

Fig. 14. Calculated (a) von Mises strain distribution (b) precipitate size distribution, for three differently textured RVE, after deformation to 18% (150 °C - 1×10^{-4} s^{-1}).

Data statement

The code used to generate the data presented here is available from LightFORM github: https://github.com/LightForm-group/Damask-KWN

Acknowledgements

The authors are grateful to the EPSRC, UK for financial support through the associated programme grant LightFORM (EP/R001715/1). The authors would like to acknowledge the assistance given by Research IT and the use of the Computational Shared Facility at The University of Manchester. MB would like to thank Elliot Cooksey-Nash for providing EBSD data and Thomas Jailin for his help with RVE generation.

References

[1] H.J. Roven, M. Liu, J.C. Werenskiold, Dynamic precipitation during severe plastic deformation of an Al-Mg-Si aluminium alloy, Mater. Sci. Eng. A 483–484 (2008) 54–58.
[2] A. Deschamps, G. Fribourg, Y. Bréchet, J.L. Chemin, C.R. Hutchinson, In situ evaluation of dynamic precipitation during plastic straining of an Al-Zn-Mg-Cu alloy, Acta Mater. 60 (2012) 1905–1916.
[3] M. Legros, G. Dehm, E. Arzt, T.J. Balk, Observation of giant diffusivity along dislocation cores, Science 319 (2008) 1646–1649.
[4] L. Couturier, A. Deschamps, F. De Geuser, F. Fazeli, W.J. Poole, An investigation of the strain dependence of dynamic precipitation in an Al-Zn-Mg-Cu alloy, Scr. Mater. 136 (2017) 120–123.
[5] C.R. Hutchinson, F. De Geuser, Y. Chen, A. Deschamps, Quantitative measurements of dynamic precipitation during fatigue of an Al-Zn-Mg-(Cu) alloy using small-angle X-ray scattering, Acta Mater. 74 (2014) 96–109.
[6] J.R. Mianroodi, P. Shanthraj, A.K. da Silva, B. Svendsen, D. Raabe, Combined modeling and experimental characterization of Mn segregation and spinodal decomposition along dislocation lines in Fe-Mn alloys, Acta Mater. (2022) https://arxiv.org/abs/2206.03767 submitted for publication.
[7] J.D. Embury, A. Deschamps, Y. Brechet, The interaction of plasticity and diffusion controlled precipitation reactions, Scr. Mater. 49 (2003) 927–932.
[8] J.D. Robson, Deformation enhanced diffusion in aluminium alloys, Metall. Mater. Trans. A 51 (2020) 5401–5413.
[9] W. Sun, Y. Zhu, R. Marceau, L. Wang, Q. Zhang, X. Gao, C. Hutchinson, Precipitation strengthening of aluminum alloys by room-temperature cyclic plasticity, Science 363 (2019) 972–975.
[10] Y.L. Li, C.P. Kohar, W. Muhammad, K. Inal, Precipitation kinetics and crystal plasticity modeling of artificially aged AA6061, Int. J. Plast. 152 (2022) 103241.
[11] D. Hull, D.J. Bacon, Introduction to Dislocations, http://dx.doi.org/10.1016/C2009-0-64358-0.
[12] M.J. Starink, S.C. Wang, A model for the yield strength of overaged Al-Zn-Mg-Cu alloys, Acta Mater. 51 (2003) 5131–5150.
[13] A. Deschamps, Y. Brechet, Influence of predeformation and ageing of an Al-Zn-Mg alloy-II. Modeling of precipitation kinetics and yield stress, Acta Mater. 47 (1998) 293–305.
[14] P. Shanthraj, P. Eisenlohr, M. Diehl, F. Roters, Int. J. Plast. 66 (2015) 31–45.
[15] P. Shanthraj, M. Diehl, P. Eisenlohr, F. Roters, D. Raabe, Spectral Solvers for Crystal Plasticity and Multi-Physics Simulations, Springer Singapore, 2019, pp. 1347–1372.
[16] F. Roters, M. Diehl, P. Shanthraj, P. Eisenlohr, C. Reuber, S.L. Wong, T. Maiti, A. Ebrahimi, T. Hochrainer, H.O. Fabritius, S. Nikolov, M. Friák, N. Fujita, N. Grilli, K.G. Janssens, N. Jia, P.J. Kok, D. Ma, F. Meier, E. Werner, M. Stricker, D. Weygand, D. Raabe, DAMASK the Düsseldorf Advanced Material Simulation Kit for modeling multi-physics crystal plasticity, thermal, and damage phenomena from the single crystal up to the component scale, Comput. Mater. Sci. 158 (2019) 420–478.
[17] D. Raabe, Y. Wang, F. Roters, Crystal plasticity simulation study on the influence of texture on earing in steel, Comput. Mater. Sci. 34 (2005) 221–234.
[18] Y.L. Li, C.P. Kohar, R.K. Mishra, K. Inal, Int. J. Plast. 132 (2020) 102759.
[19] J. Wang, Q. Li, C. Xiong, Y. Li, B. Sun, Effect of Zr on the martensitic transformation and the shape memory effect in Ti-Zr-Nb-Ta high-temperature shape memory alloys, J. Alloys Compd. 737 (2018) 672–677.
[20] H. Chen, Z. Chen, G. Ji, S. Zhong, H. Wang, A. Borbély, Y. Ke, Y. Bréchet, Experimental and modelling assessment of ductility in a precipitation hardening AlMgScZr alloy, Int. J. Plast. 139 (2021) 102971.
[21] N. Anjabin, A. Karimi Taheri, H.S. Kim, Crystal plasticity modeling of the effect of precipitate states on the work hardening and plastic anisotropy in an Al-Mg-Si alloy, Comput. Mater. Sci. 83 (2014) 78–85.
[22] S. Ghorbanpour, M. Zecevic, A. Kumar, M. Jahedi, J. Bicknell, L. Jorgensen, I.J. Beyerlein, M. Knezevic, Int. J. Plast. (2017) 162–185.
[23] D.A. Porter, K.E. Easterling, K.E. Easterling, Phase transformations in metals and alloys (Revised reprint), 2009, http://dx.doi.org/10.1201/9781439883570.
[24] P. Guyot, L. Cottignies, Precipitation kinetics, mechanical strength and electrical conductivity of AlZnMgCu alloys, Acta Mater. 44 (1996) 4161–4167.
[25] J.D. Robson, M.J. Jones, P.B. Prangnell, Extension of the N-model to predict competing homogeneous and heterogeneous precipitation in Al-Sc alloys, Acta Mater. 51 (2003) 1453–1468.
[26] C.R. Hutchinson, Modeling the Kinetics of Precipitation in Aluminium Alloys in Fundamentals of Aluminium Metallurgy: Production, Processing and Applications, Woodhead Publishing Limited, 2010, pp. 422–467.
[27] A. Deschamps, C.R. Hutchinson, Precipitation kinetics in metallic alloys: Experiments and modeling, Acta Mater. 220 (2021) 117338.
[28] X. Xu, J. Zheng, Z. Li, R. Luo, B. Chen, Precipitation in an Al-Zn-Mg-Cu alloy during isothermal aging: Atomic-scale HAADF-STEM investigation, Mater. Sci. Eng. A 691 (2017) 60–70.
[29] M. Militzer, W.P. Sun, J.J. Jonas, Modelling the effect of deformation-induced vacancies on segregation and precipitation, Acta Metall. Mater. 42 (1994) 133–141.
[30] S. Khani Moghanaki, M. Kazeminezhad, Modeling of the mutual effect of dynamic precipitation and dislocation density in age hardenable aluminum alloys, J. Alloys Compd. 683 (2016) 527–532.
[31] M. Bignon, P. Shanthraj, J.D. Robson, Modelling dynamic precipitation in pre-aged aluminium alloys under warm forming conditions, Acta Mater. 234 (2022) 118036.
[32] L.M. Cheng, W.J. Poole, J.D. Embury, D.J. Lloyd, The influence of precipitation on the work-hardening behavior of the aluminum alloys AA6111 and AA7030, Metall. Mater. Trans. A 34 (2003) 2473–2481.
[33] F. Roters, P. Eisenlohr, L. Hantcherli, D.D. Tjahjanto, T.R. Bieler, D. Raabe, Overview of constitutive laws, kinematics, homogenization and multiscale methods in crystal plasticity finite-element modeling: Theory, experiments, applications, Acta Mater. 58 (2010) 1152–1211.
[34] A. Deschamps, F. De Geuser, Z. Horita, S. Lee, G. Renou, Precipitation kinetics in a severely plastically deformed 7075 aluminium alloy, Acta Mater. 66 (2014) 105–117.
[35] M. Perez, M. Dumont, D. Acevedo-Reyes, Implementation of classical nucleation and growth theories for precipitation, Acta Mater. 56 (2008) 2119–2132.
[36] K.L. Murty, K. Detemple, O. Kanert, J.T.M. Dehosson, In-situ nuclear magnetic resonance investigation of strain, temperature, and strain-rate variations of deformation-induced vacancy concentration in aluminum, Metall. Mater. Trans. A 29 (1998) 153–159.

[37] Z. Ma, Strain Path Effects on Dynamic Precipitation in Aluminium Alloys (Ph.D. thesis), University of Manchester, 2023 in press.
[38] G. Fribourg, Y. Bréchet, A. Deschamps, A. Simar, Microstructure-based modelling of isotropic and kinematic strain hardening in a precipitation-hardened aluminium alloy, Acta Mater. 59 (2011) 3621–3635.
[39] Y. Du, Y.A. Chang, B. Huang, W. Gong, Z. Jin, H. Xu, Z. Yuan, Y. Liu, Y. He, F.Y. Xie, Diffusion coefficients of some solutes in fcc and liquid Al: Critical evaluation and correlation, Mater. Sci. Eng. A 363 (2003) 140–151.
[40] E. Cooksey-Nash, (Ph.D. thesis), University of Manchester, 2023 in press.
[41] S. Dumoulin, L. Tabourot, Experimental data on aluminium single crystals behaviour, Proc. Inst. Mech. Eng. C (2005) 1159–1167.
[42] G. Fribourg, A. Deschamps, Y. Bréchet, Precipitation strengthening in AA7449 aluminium alloy: Understanding the relationship between microstructure, yield strength and strain hardening, Mater. Sci. Forum 519–521 (2006) 991–996.
[43] A. Considère, Annales des Ponts et Chaussés, 1885, pp. 574–775.
[44] W.Z. Han, Y. Chen, A. Vinogradov, C.R. Hutchinson, Dynamic precipitation during cyclic deformation of an underaged Al-Cu alloy, Mater. Sci. Eng. A 528 (2011) 7410–7416.
[45] C.R. Hutchinson, P.T. Loo, T.J. Bastow, A.J. Hill, J. da Costa Teixeira, Quantifying the strain-induced dissolution of precipitates in Al alloy microstructures using nuclear magnetic resonance, Acta Mater. 57 (2009) 5645–5653.
[46] W. Xin-yun, H.E. Hu, X. Ju-chen, Effect of deformation condition on plastic anisotropy of as-rolled 7050 aluminum alloy plate, Mater. Sci. Eng. A 515 (2009) 1–9.
[47] W.U. Mirihanage, J.D. Robson, S. Mishra, P. Hidalgo-Manrique, J.Q. da Fonseca, C.S. Daniel, P.B. Prangnell, S. Michalik, O.V. Magdysyuk, T. Connolley, M. Drakopoulos, Direct observation of the dynamic evolution of precipitates in aluminium alloy 7021 at high strain rates via high energy synchrotron X-rays, Acta Mater. 205 (2021) 116532.
[48] K. Teichmann, C.D. Marioara, K.O. Pedersen, K. Marthinsen, The effect of simultaneous deformation and annealing on the precipitation behaviour and mechanical properties of an Al-Mg-Si alloy, Mater. Sci. Eng. A 565 (2013) 228–235.
[49] Dream3D manual, 2023, http://www.dream3d.io.
[50] D. Raabe, M. Sachtleber, Z. Zhao, F. Roters, S. Zaefferer, Micromechanical and macromechanical effects in grain scale polycrystal plasticity experimentation and simulation, Acta Mater. 49 (2001) 3433–3441.